Heteronuclear and Homonuclear Radio Frequency Driven Recoupling

Authors: Evgeny Nimerovsky*, Kai Xue, Kumar Tekwani Movellan & Loren B. Andreas*

Affiliations:

Department of NMR based Structural Biology, Max Planck Institute for Biophysical Chemistry, Am Fassberg 11, Göttingen, Germany

*Corresponding authors: land@nmr.mpibpc.mpg.de ORCID: 0000-0003-3216-9065 and evni@nmr.mpibpc.mpg.de

Abstract

The Radio Frequency Driven Recoupling (RFDR) pulse sequence is used in magic-angle spinning (MAS) NMR to recouple homonuclear dipolar interactions. Here we show simultaneous recoupling of both the heteronuclear and homonuclear dipolar interactions by applying RFDR pulses on two channels. We demonstrate the method, called HETeronuclear RFDR (HET-RFDR) on microcrystalline SH3 samples at 10 kHz and 55.555 kHz MAS. Numerical simulations of both HET-RFDR and standard RFDR sequences allow better understanding of the influence of offsets, paths of magnetization transfers for both HET-RFDR and RFDR experiments as well as the crucial role of XY phase cycling.

Keywords: Magic Angle Spinning NMR, heteronuclear and homonuclear RFDR, the operator analysis

Introduction

Magic-angle spinning (MAS) NMR spectroscopy is used to obtain atomic resolution spectra of materials and biological molecules in the solid state, by removal of the broadening associated with anisotropic dipolar couplings and other interactions. Under control of radio frequency pulses, dipolar

22   interactions can be switched on, or recoupled, in order to correlate nearby spins or to accurately determine

23   internuclear distances. Recoupling sequences can be broadly categorized as homonuclear (Meier and Earl,

24   1986; Tycko and Dabbagh, 1990; Gullion and Vega, 1992; Bennett et al., 1992; Ok et al., 1992; Zhang et

25   al., 2020; Gelenter et al., 2020; Takegoshi et al., 2001; Szeverenyi et al., 1982; Hou et al., 2011b, 2013;

26   Carravetta et al., 2000; Bennett et al., 1998; Nielsen et al., 2012) or heteronuclear (Gelenter et al., 2020;

27   Gullion and Schaefer, 1989; Jaroniec et al., 2002; Hing et al., 1992; Hartmann and Hahn, 1962; Rovnyak,

28   2008; Metz et al., 1994; Hediger et al., 1994; Hou et al., 2011a; Brinkmann and Levitt, 2001; Gelenter and

29   Hong, 2018; Zhang et al., 2016; Nielsen et al., 2012).

30   The recoupling of the homonuclear dipolar interactions with a train of π-pulses every rotor period

31   was originally introduced by Gullion and Vega (Gullion and Vega, 1992) and Bennett et all (Bennett et al.,

32   1992). Since, the homonuclear Radio Frequency Driven Recoupling (RFDR) sequence (Bennett et al.,

33   1992) has been successfully applied for the qualitative and quantitative determinations of the dipolar spin

34   correlations in materials (Saalwächter, 2013; Messinger et al., 2015; Fritz et al., 2019; Roos et al., 2018;

35   Nishiyama et al., 2014a; Wong et al., 2020; Hellwagner et al., 2018; Pandey and Nishiyama, 2018) and

36   biomolecular samples (Zheng et al., 2007; Tang et al., 2011; Shen et al., 2012; Pandey et al., 2014; Grohe

37   et al., 2019; Andreas et al., 2015; Petkova et al., 2002; Aucoin et al., 2009; Zinke et al., 2018; Zhang et al.,

38   2017; Zhou et al., 2012; Jain et al., 2017; Colvin et al., 2015; Shi et al., 2015; Daskalov et al., 2020). Sun

39   et al. (1995) showed that the RFDR pulse sequence element could also be used as a part of the SPICP

40   experiment (Wu and Zilm, 1993) for removing the undesired effect of the chemical shift terms to zero order.

41   Depending on the assumptions (Bennett et al., 1992; Gullion and Vega, 1992; Ishii, 2001), two

42   different Average Hamiltonian Theory (Haeberlen and Waugh, 1968; Maricq, 1982) (AHT) descriptions

43   have been detailed for RFDR. In both, homonuclear dipolar recoupling occurs via a rotor-synchronized

44   train of π-pulses, with one pulse each rotor period (Bennett et al., 1992) on a single channel. In the first

45   case, delta π-pulses are assumed (Bennett et al., 1992). The efficiency of recoupling is linked with the

46   rotational resonance conditions (Bennett et al., 1992, 1998), and depends on the ratio between chemical

47   shift offset difference and MAS rate. In the second theoretical description, the effects of finite π-pulses are

48   considered (Bennett et al., 1992; Ishii, 2001; Nishiyama et al., 2014b; Zhang et al., 2015; Brinkmann et al.,

49   2002; Ji et al., 2020). The efficiency of recoupling in this case depends on a duty factor (Ishii, 2001), defined

50   as the fraction of the rotor period occupied by the π-pulse. The RFDR pulses are applied according to a

51   variety of XY phase cycling schemes, which have been analyzed with the intent to suppress imperfections

52   associated with offset differences, rf-field inhomogeneity and second order Average Hamiltonian terms

53   between different anisotropic interactions (Zhang et al., 2015).

54   The full high field truncated dipolar Hamiltonian of the homonuclear I_2 spin system is represented

55   as follows:

$$H_{D,Full}^{II} = \omega_{D,12}(t)[3I_{z1}I_{z2} - \bar{I}_1 \cdot \bar{I}_2]. \quad \text{Eq. (1)}$$

57   where $\omega_{D,12}(t)$ is a periodic time dependent function (Olejniczak et al., 1984) that depends on the

58   positions of spins I_1 and I_2 within the rotor. This Hamiltonian is subsequently referred to as the full

59   Hamiltonian, and contains only the A and B terms of the dipolar alphabet (Slichter, 1990).

60   The interesting conclusion can be obtained, if we simplify the Eq. (1). The dipolar Hamiltonian

61   during RFDR can be simplified (in the absence of other interactions) by considering that $\bar{I}_1 \cdot \bar{I}_2$ commutes

62   with the secular part $(I_{z1}I_{z2})$ and with the rf-field Hamiltonian. At the end of each rotor period, the

63   oscillatory $\omega_{D,12}(t)$ term ensures zero total evolution. The simplified Eq. (1) is:

$$H_{D,M}^{II} = 1.5\omega_{D,12}(t)2I_{z1}I_{z2}. \quad \text{Eq. (2)}$$

65   Comparing Eq. (2) with full Dipolar Hamiltonian of the heteronuclear IS spin system(Mehring, 1983):

$$H_{D,Full}^{IS} = \omega_{D,12}(t)2I_zS_z, \quad \text{Eq. (3)}$$

67   we notice that the difference between Eq. (3) and Eq. (1) is a factor of 1.5. Note that we have made the

68   substitution of I_{z1} to I_z and I_{z2} to S_z while the dipolar function, $\omega_{D,12}(t)$, has been kept the same. Such

69   comparison suggests a HETeronuclear-RFDR (HET-RFDR), which should have a scaling of 1.5 as

70   compared with the homonuclear case.

71   In this article we investigate spin dynamics under HET-RFDR, in which RFDR π-pulses are

72   applied simultaneously on two channels (Figure 1). We demonstrate simultaneous heteronuclear and

73   homonuclear transfers using HET-RFDR applied to α-PET (Movellan et al., 2019) labeled SH3 at 10 kHz

74   and 55.555 kHz MAS.

75   We perform and compare a numerical operator analysis of both RFDR and HET-RFDR

76   experiments under different simulated conditions. This numerical analysis allows to define the conditions

77   under which homonuclear and heteronuclear RFDR polarization transfers have similar behaviors, to

78   understand the paths through which the signals are transferred between operators, and to understand the

79   crucial role of 90 degree phase alternation (XY-4, XY-8, etc) (Ishii, 2001; Nishiyama et al., 2014b; Zhang

80   et al., 2015; Hellwagner et al., 2018) for both RFDR and HET-RFDR recoupling.

81   **HET-RFDR Experiments**

82   Figure 1 shows two 2D (H)N(H)H pulse sequences used to evaluate the HET-RFDR transfer. For

83   both sequences, the transfer from proton to nitrogen is implemented with ramped cross polarization (CP)

84   and then the nitorgen dimension is encoded (t_1) for 2D spectra. In Figure 1a, the transfer to structurally

85   interesting protons is implemented with N to H CP followed by H-H RFDR. In Figure 1b, the same

86   transfer is implemented with a single HET-RDFR period. The HET-RFDR transfer avoids the back CP

87   step. Instead, nitrogen polarization is placed along the $\hat{z}$ axis and transfered to directly bonded proton

88   spins and at the same time to remote proton spins with the simultaneous application of the π-pulses on the

89   proton and nitrogen channels.
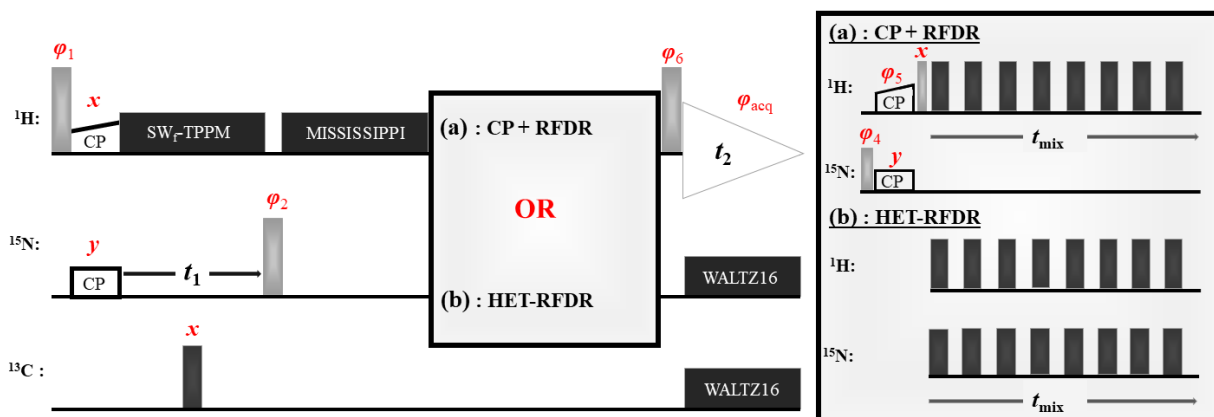
Figure 1 Two versions of the (H)N(H)H pulse sequence are shown. The first, (a), is the standard implementation with CP + RFDR. The second, (b), instead uses the new HET-RFDR recoupling element. Light grey pulses represent π/2-pulses, whereas dark grey pulses represent π-pulses. The ramped CP transfer from proton to nitrogen as well as from nitrogen to proton in (a) are indicated with constant power on the nitrogen channel and a ramp in power on the proton chanenl. During the inderect dimension (t_1), SW$_f$-TPPM decoupling is applied at 55 kHz , repectively. A single π-pulse in the middle of t_1 decouples carbon. Water supression is implemented with the MISSISSIPI (Zhou and Rienstra, 2008) sequence. During acquisition, WALTZ16 (Thakur et al., 2006) decoupling is applied on nitrogen and carbon channels. The phases are: $\varphi_1 = x, -x$; $\varphi_{acq} = y, -y, -y, y, -y, y, y, -y$. In (a) the phases are: $\varphi_2 = x$; $\varphi_4 = x, x, -x, -x$; $\varphi_5 = y, y, y, y, -y, -y, -y, -y$; $\varphi_6 = x$. In (b) the phases are: $\varphi_2 = x, x, -x, -x$; $\varphi_6 = x, x, x, x, -x, -x, -x, -x$. RFDR π-pulses on both channels use the XY8 scheme (Gullion et al., 1990).

Figure 2 compares the 1D and 2D spectra obtained with the two sequences of Figure 1. In Figure 2a, the 1D signal is shown as a function of RFDR mixing time. For the standard sequence (blue) the N to H CP was 0.55 ms. The HET-RFDR signal is shown in (red). Without RFDR mixing, the CP+RFDR detects directly bonded amide protons (Figure 2a, red with zero mixing time) and zero signal occurs for HET-RFDR (Figure 2a, blue with zero mixing time) since the signal is on nitrogen. With increasing RFDR mixing, the signal is transferred from directly bonded amide protons to remote protons for the CP+RFDR sequence (red), whereas simultaneous transfer from nitrogen spins to amide protons and from amide protons to remote protons occurs with HET-RFDR (blue). For the directly bonded amide protons, the HET-RFDR polarization transfer achieves only ~40% of the CP signal. This occurs at 0.846 ms mixing (second red spectrum). However, with increased mixing of about 3 ms, HET-RFDR reaches the

110 same efficiency as the standard sequence. This is notable since transfer over long distances has been

111 implemented with ~3 ms mixing for deuterated samples (Grohe et al., 2019; Linser et al., 2014).

112   Structurally interesting cross-peaks are indeed observed in the 2D HET-RFDR spectrum shown in

113 Figure 2b at 3.456 ms mixing. For example, we have observe the amide-amide contact between V44 and

114 V53, which is 4.82 Å in the crystal (pdb code 2NUZ (Castellani et al., 2002)). The amide to side chain

115 contact of a A55 N to Hβ (3.41 Å) is also indicated in the Figure, along with a sequential contact from

116 Y13 ^{15}N to L12 ^{1}Hα, which is 3.26 Å. These peaks are boxed in Figure 2b, and the 1D slices shown above

117 the 2D spectra. For comparison, in 1D slices we show CP +RFDR (blue) and HET-RFDR (red) intensities

118 of these three peaks for two different mixing times: 1.154 ms (dashed) 3.456 ms (solid). Both methods

119 provide similar intensities at long mixing time, whereas at shorter mixing times CP+RFDR provides

120 higher intensities for short range distances.
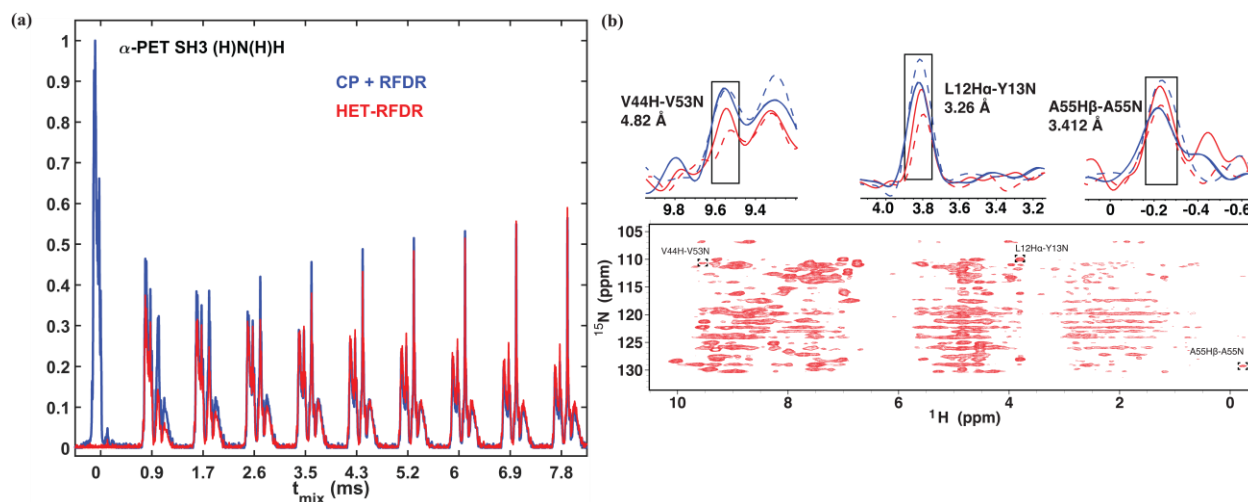
121

122 **Figure 2** 1D (a) and 2D (b) (H)N(H)H spectra of α-PET labeled SH3. For all spectra the first CP from proton to nitrogen was

123 performed with 1.05 ms. (a) 1D spectra with different sequences used for the second transfer: CP + RFDR (blue) and HET-RFDR

124 (red). For CP + RFDR, 0.55 ms of CP was used. For both RFDR and HET-RFDR, t_{mix} of 0, 0.846, 1.728, 2.592, 3.456, 4.32,

125 5.184, 6.048, 6.912, 7.7776 msare shown. (b) 2D HET-RFDR at 3.456 ms of mixing time. Spectra were recorded at a 600 MHz

126 Bruker instrument equiped with a 1.3 mm probe and an MAS frequency of 55 kHz. The widths of π-pulses on proton and

127 nitrogen channels were 5.8 us and 6.6 us, respectively. The 1D slices show the intensities of three selected peaks. CP+RFDR

128   (blue) and HET-RFDR (red) at 1.154 ms (dashed lines) and 3.456 ms (solid lines) mixing are displayed. The experimental

129   parameters are detailed in Table 1 and 2 the 'Experimental Methods'. XY8 phase cycling was used.

130   At 55.555 kHz MAS on a 600 MHz instrument, the chemical shift offsets can always be much

131   smaller than the spinning frequency. At a lower MAS frequency, the offsets become important for HET-

132   RFDR. The recoupling then depends on a heteronuclear 'offset difference' that we define as $\Delta\Omega_{ij} = \Omega_i -$

133   Ω_j, where Ω_i and Ω_j are the offsets on each channel (the difference between the Larmor frequency of the

134   spin and the carrier frequency (Bak et al., 2000)). When $\Omega_i = \Omega_j = 0$ as well as $\Delta\Omega_{ij} = \Omega_i - \Omega_j \approx n\nu_R$

135   (n=0, ±1, ±2…), the HET-RFDR polarization transfer reaches local maximal intensities. However, when

136   $\Delta\Omega_{ij} = \Omega_i - \Omega_j \approx 0.5n\nu_R$ (n=±1, ±3…), the HET-RFDR polarization transfer reaches local minima. The

137   experimental confirmation of this is shown in Figure 3, where the effect of different proton and carbon

138   offsets is explored for proton-carbon HET-RFDR spectra. The spinning frequency was reduced to 10 kHz

139   MAS for these measurements and the signal detected on the carbon channel. The 1D HC HET-RFDR

140   pulse sequence is shown in the SI (Figure S1).

141   Figures 3a-e depicts the HET-RFDR spectra when the carbon carrier frequency is changed

142   (numbers show the offset from the alpha carbon at ~53 ppm), whereas the alpha proton offset is kept at 0

143   kHz (at 4.6 ppm). While heteronuclear transfer is detected at zero offset (Figure 3a) or with 11.1 kHz

144   carbon offset (Figure 3e), the signal remains in the noise when the carbon offset is 5.85 kHz (Figure 3c).

145   A similar effect can be detected when the proton carrier frequency is changed (increased from 4.6 ppm),

146   but this time the carbon offset is set to 5 kHz from Cα (83.66 ppm) to show that it is the offsets on both

147   channels ($\Delta\Omega_{C\alpha H\alpha}$) that is important (Figures 3f-j). The series of spectra show a local minimal transfers at

148   offset differences of 5 kHz (Figure 3f) and -5 kHz (Figure 3h) and local maximal polarization transfers at

149   differences of 0 (Figure 3g) and -10 kHz (Figure 3j).
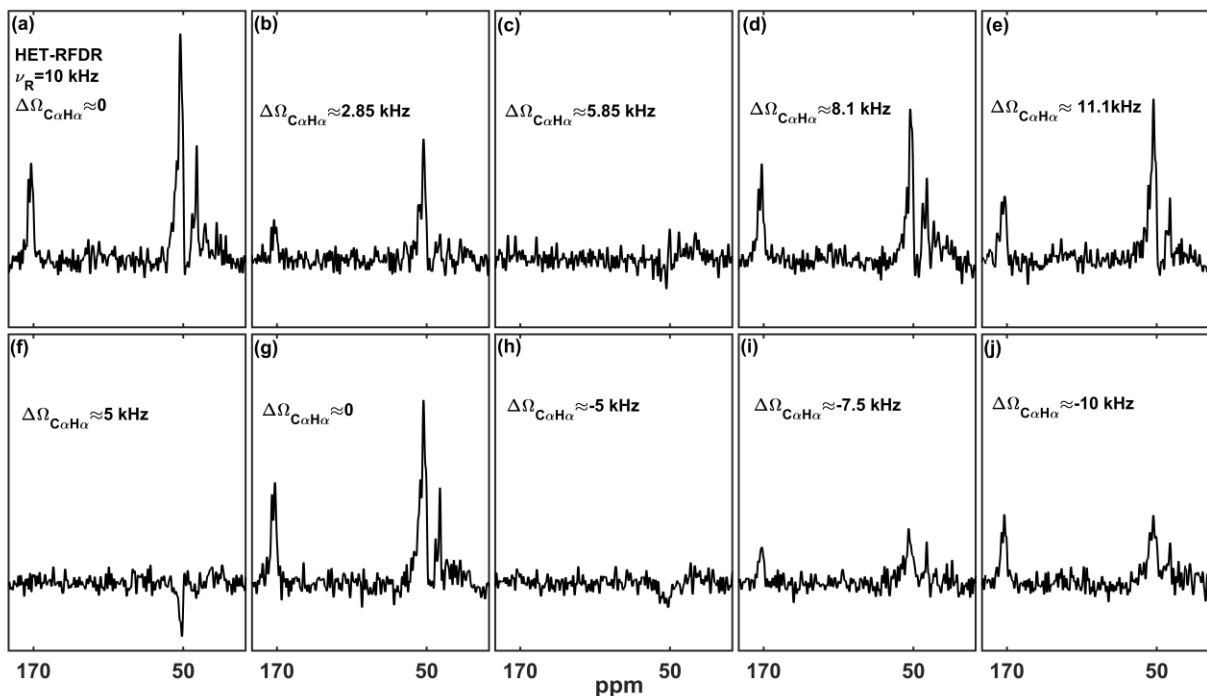
150

151   **Figure 3** The influence of the carbon and proton offsets on proton-carbon HET-RFDR polarization transfers at 4.8 ms mixing.

152   α-PET labeled SH3 was used with 10 kHz MAS at a 600 MHz spectrometer using a 1.3 mm probe. The widths of π-pulses on

153   proton and carbon channels were 5.8 us and 6.6 us, respectively. For (a)-(e) the proton carrirer frequency was set to 4.6 ppm and

154   carbon carrier frequency was set to 51 ppm (a), 70 ppm (b), 90 ppm (c), 105 ppm (d) 125 ppm (e). For (f)-(j) the carbon carrirer

155   frequency was set to 83.66 ppm and the proton carrier frequency was set to 4.6 ppm (f), 12.933 ppm (g), 21.26 ppm (h), 25.43

156   ppm (i) and 29.6 ppm (j). The indicated offset differences, $\Delta\Omega_{C\alpha H\alpha} = \Omega_{C\alpha} - \Omega_{H\alpha}$ in kHz were calculated based on typical

157   isotropic chemical shifts of C_α (51 ppm) and H_α (4.6 ppm) at a 600 MHz spectrometer. The experimental parameters are detailed

158   in Table 1 and 2 the 'Experimental Methods'. The 1D HET-RFDR sequence is shown in the SI (Figure S1). XY8 phase cycling

159   was used.

160   **Numerical Operator Analysis**

161   To comprehend the mechanism underlying the transfers during the HET-RFDR and also the well-

162   known RFDR pulse sequence, we use a numerical simulation approach. We identify the conditions under

163   which the heteronuclear and homonuclear spin systems under HET-RFDR and RFDR sequences have

164   similar behaviors. Considering the evolutions of the different spin systems through HET-RFDR and

165 RFDR during the first two rotor periods, we identify the operators that are involved in the polarization

166 transfer.

167   To identify the conditions under which the HET-RFDR and RFDR sequences have similar and

168 different behaviors we simulated a three spin system at high (55.555 kHz) and low (10 kHz) MAS

169 frequencies. In Figure 4 we compare the RFDR transferred signals for I_3 (a homonuclear 3-spin system,

170 black lines) and HET-RFDR transferred signals for *ISR* (three different types of spins with the names *I*, *S*

171 and *R*; red lines) spin systems. At 55.555 Hz MAS when the offset difference is small compared to MAS

172 rate, the behavior of the homonuclear I_3 spin system is similar to the behavior of the heteronuclear *ISR*

173 spin system (Figure 4a). However, when the MAS rate is low (10 kHz) and the offset difference cannot be

174 neglected, the behaviors of these spin systems are completely different (Figure 4b). For the homonuclear

175 spin system (I_3), the polarization transfers are efficient for all dipolar pairs (black lines), whereas for the

176 heteronuclear spin system (*ISR*) the HET-RFDR polarization transfer is detected between *R* and *I* spins

177 (Figure 4b, red dashed-dotted line) only. For this *RI* pair the offset difference was chosen as 10 kHz,

178 whereas for the other spin pairs (*SI*, *RS*) the offset differences were set to 5 kHz. These simulations show

179 a special condition of $\sim0.5\nu_R$ of offset difference for the heteronuclear spins under which the transfer

180 obtains local / global minima values. The simulations are in full agreement with the experiments, which

181 were shown in Figure 3. Another interesting observation can be made from the influence of the offset

182 difference on the RFDR transfer for the homonuclear I_3 spin system (Figure 4b, black lines). For a 5 kHz

183 of offset difference, the RFDR polarization transfer between I_{z2} and I_{z3} spins is significantly faster with 10

184 kHz MAS (Figure 4b, black dashed line) than at 55.555 kHz MAS (Figure 4a, black dashed line). Since

185 the duty factor is decreased with decreasing MAS frequency(Ishii, 2001): 0.33 for 55.555 kHz MAS and

186 0.06 for 10 kHz MAS, the opposite behavior is expected if one considers only the effect of finite pulses in

187 the RFDR experiment(Ishii, 2001). It indicates that when the offset difference cannot be neglected with

188 respect to the MAS rate, it has a significant influence on the RFDR transfer efficiency between

9

189 homonuclear spins despite the significant remoteness from the rotational resonance condition (Bennett et

190 al., 1992, 1998).
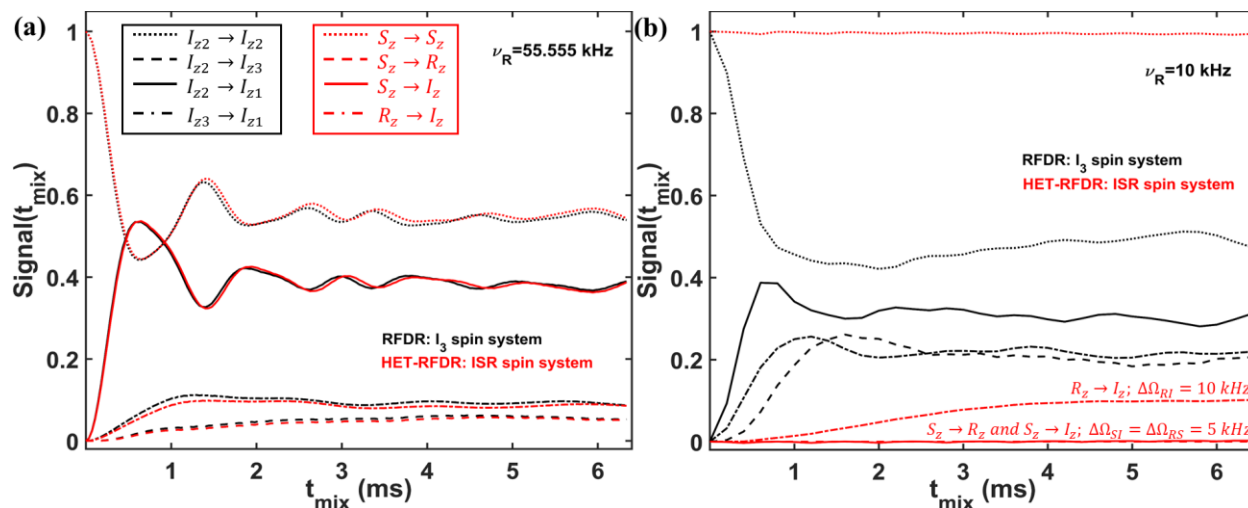
191

192 **Figure 4** Comparison of the simulated RFDR and HET-RFDR signals. I_3 (three homonuclear spins, black lines) and *ISR* (three

193 different spin types, red lines) for 55.555 kHz (a) and 10 kHz (b) MAS. 83 kHz of rf-field is used (6 us of the widths of π-pulses).

194 The vertical axis shows the intensities of the starting and transferred signals between different operators of I_3 and *ISR* spin

195 systems, respectively (the initial operator → the measured operator): $I_{z2} \rightarrow I_{z2}$ and $S_z \rightarrow S_z$ – (the dotted lines); $I_{z2} \rightarrow I_{z3}$ and

196 $S_z \rightarrow R_z$ – (the dashed lines); $I_{z2} \rightarrow I_{z1}$ and $S_z \rightarrow I_z$ – (the solid lines); $I_{z3} \rightarrow I_{z1}$ and $R_z \rightarrow I_z$ – (the dashed-dotted lines). For

197 both spin systems the offset (Ω) and CSA values are: [-3; 2; 7] (kHz) and [5.2; 2.5; 3].The dipolar coupling constants for

198 homonuclear spin system ($I_{3)}$ spin system are: $\nu_{12,D} = 7.333$ kHz, $\nu_{13,D} = 2$ kHz, $\nu_{23,D} = 0.333$ kHz. For *ISR* spin system all

199 dipolar constants are 1.5 times larger: $\nu_{IS,D} = 11$ kHz, $\nu_{IR,D} = 3$ kHz, $\nu_{SR,D} = 0.5$ kHz. The simulated measurements occurs

200 every 2 rotor periods. XY8 phase cycling is used. $I_{z1} \rightarrow I_{z1}, I_{z3} \rightarrow I_{z3}, I_z \rightarrow I_z$ and $R_z \rightarrow R_z$ are not shown.

201   In order to understand via which operators the polarization transfer occurs, we considered the

202 evolutions of two systems - I_2 homonuclear and *IS* heteronuclear spin systems - under RFDR and HET-

203 RFDR sequences with 10 kHz MAS. We simulated the polarization transfers between different operators

204 during the first two rotor periods, which completes the basic RFDR element: $t(\pi_x) \rightarrow del_1 \rightarrow t(\pi_y) \rightarrow$

205 del_2. We consider the amplitudes of the operators for a single molecular orientation since it allows to see

206 the significant evolution of the operators during the two rotor periods. Figure 5a,c,e shows the amplitudes

207 of four Cartesian operators (Ernst et al., 1987) for *IS* (HET-RFDR) and Figures 5b,d,f shows the operators

208 for I_2 (RFDR) spin systems. The measured Cartesian operators are $I_z, S_z, 2I_xS_y, 2I_yS_x$ and

209 $I_{z1}, I_{z2}, 2I_{x1}I_{y2}, 2I_{y1}I_{x2}$ for IS and I_2 spin systems, respectively.

210 The evolutions of four operators *during* two rotor periods for the IS spin system the I_2 spin system are

211 different, regardless of the offset difference. However, with a zero offset difference, the simulated

212 heteronuclear operators (Figure 5a) and the homonuclear operators (Figure 5b) show the same values of

213 the amplitudes at one and two rotor periods. From the 64 possibilites (details in the SI, section 'The

214 Operator Paths') for magnetization tranfer between heteronuclear operators I_z and S_z during the two rotor

215 periods, we find only one path with nonzero amplitude: $I_z \xrightarrow{\pi_x} 2I_xS_y \xrightarrow{del_1} 2I_xS_y \xrightarrow{\pi_y} S_z \xrightarrow{del_2} S_z$. In contrast to

216 the single path found for HET-RFDR, for the homonuclear case all 64 paths connecting operators I_{z1} and

217 I_{z2} have non-zero amplitudes. However, after each rotor period, the sum of all homonuclear paths provides

218 the same values of the amlitudes as for the heteronuclear IS spin system.

219 In contrast, with a non-zero offset difference, the amplitudes of homonuclear and heteronuclear operators

220 do not coinside at any time (Figures 5c and d). Moreover, while the amplitude of $I_{z1} \rightarrow I_{z2}$ polarization

221 transfer is sigificantly increased (Figure 5d, green line), the corresponding heteronuclear amplitude for

222 $I_z \rightarrow S_z$ transfer is sigificantly decreased (Figure 5c, green line).

223 Figure 5c demonstrates the case, when negligible small HET-RFDR transfer is observed with $0.5\nu_R$ offset

224 difference. To understand the influence of the $0.5\nu_R$ offset difference for that case, the evolution of the

225 operators during first two rotor period is considered. During the first π_x pulse the starting signal is

226 transferred from I_z to $2I_xS_y$. Because of the offset difference of $0.5\nu_R$, the amplitude of this operator is

227 mainly transferred to $2I_yS_x$ during the first delay (Figure 5c, red line). Since the second π-pulse has phase

228 y, there is no transfer from $2I_yS_x$ to I_{z2} and very little $I_z \rightarrow S_z$ polarization transfer overall by the end of

229 the second rotor period (Figure 5c, green line).

230 In general, under $\pm \sim 0.5 n\nu_R$ (n=1,3,5,…) HET-RFDR transfer signal can obtain local minima

231 (negative signals, Figure S5 in SI), whereas under $\pm \sim n\nu_R$ offset difference the local maxima are detected.

232   The demonstrated case in Figure 5c indicates the importance of the phase cycling for RFDR and

233   HET-RFDR sequences. Figures 5d and f show the evolution of the operators when there is no offset and

234   both π-pulses have the same phase cycling – XX. For *IS* spin system (Figure 5e) only two operators have

235   nonzero amplitudes during the investigated time: I_z (black line) and $2I_xS_y$ (blue line), whereas S_z and $2I_yS_x$

236   are not created. For the I_2 spin system (Figure 5d) all four operators envolve during these two rotor

237   periods. However, by the end of two rotor periods only two operators have nonzero amplitudes, as for the

238   *IS* spin system. In neither case is there magnetization transfer from I_z to S_z nor from I_{z1} to I_{z2} after one or

239   two rotor periods. The formal proof of zero transfer signal for homonuclear two spin system in the

240   absence of offset difference can be found in the SI, "RFDR Phase Cycling" section.

241   Additional spectra and simulation results are found in the supporting information. We recorded

242   proton-carbon HET-RFDR spectra using fully protonated [^{13}C, ^{15}N] labeled SH3. We numerically

243   simulated multi-spin systems, either containing two protons and two carbons, or one nitrogen and two

244   protons, in order to track more complex transfer of magnetization. The main conclusions from the

245   simulations and the experiments in the SI are the agreement between experimental and simulated HET-

246   RFDR transfer efficiencies, and the expected small dependence of the HET-RFDR recoupling on the flip

247   angle deviations with XY8 phase cycling (Gullion et al., 1990).

248
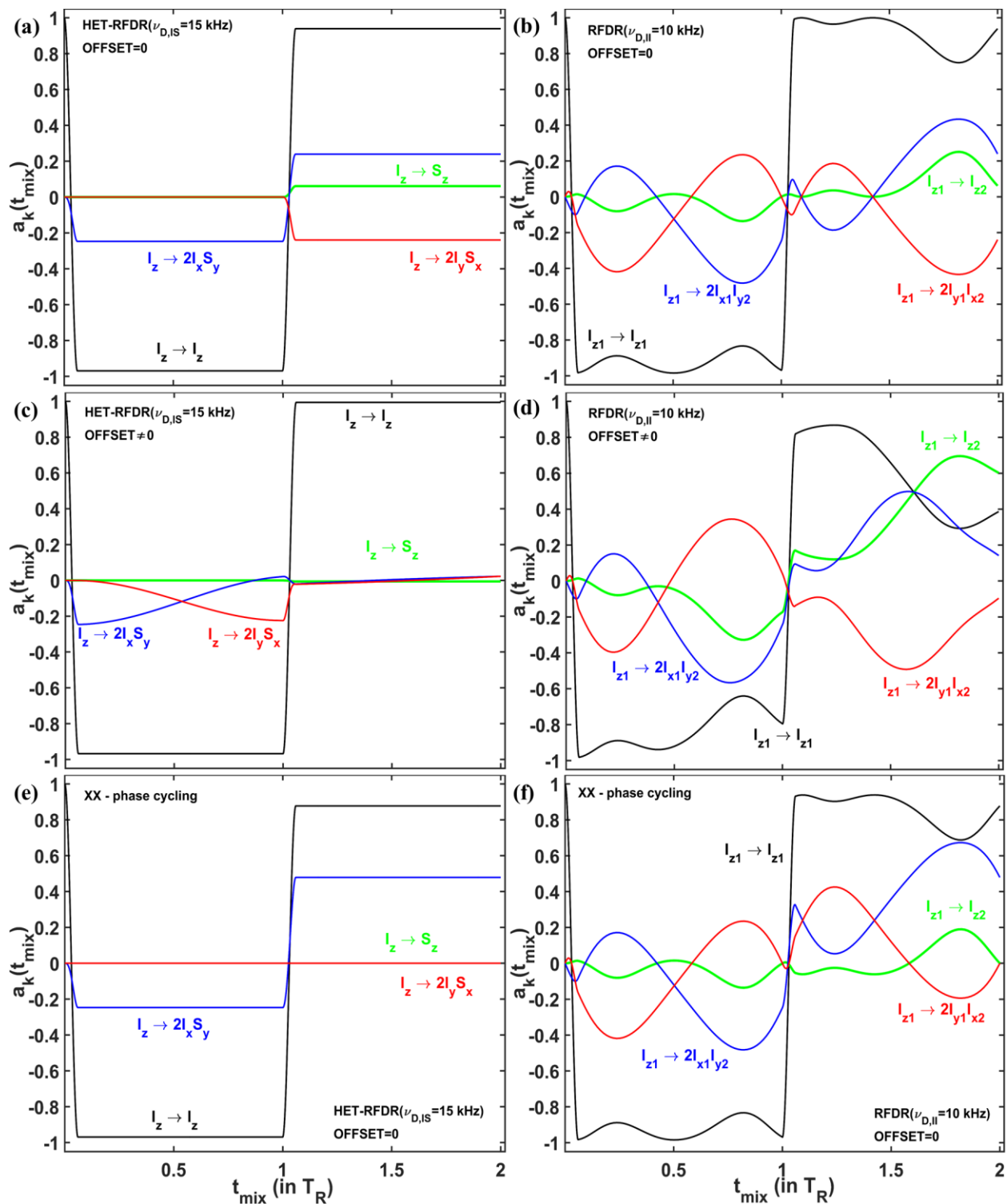
Figure 5 The operator evolution through HET-RFDR and RFDR over two rotor periods. The simulated amplitudes of the operators of a single crystal (Euler angles: 184°; 141°; 349°) for HET-RFDR ((a), (c)) and RFDR ((b), (d)). For the heteronuclear *IS* spin system, ($\nu_{D,IS} = 15$ kHz, the initial operator is I_z) and for the homonuclear I_2 spin system, ($\nu_{D,II} = 10$ kHz, the initial

252   operator is I_{z1}). The MAS frequency was 10 kHz and the rf-field was 83 kHz. Black lines – I_z and I_{z1}; Green lines – S_z and I_{z2};

253   Blue lines – $2I_xS_y$ and $2I_{x1}I_{y2}$; Red lines – $2I_yS_x$ and $2I_{y1}I_{x2}$. For (a) – (d) the phases of the first and second π-pulses are X and Y,

254   respectively. (e) and (f) show the case of IS and I_2 spin systems, respectively, when the phases of the first and second π-pulses are

255   both X. (a), (b), (e), (f) – Offset values in kHz: 0, 0. (c) and (d) – Offset values in kHz: 2, -3.

Conclusion

257   In this article we firstly demonstrated HETeronuclear RFDR recoupling, when π-pulses with XY8

258   phase cycling were applied simultaneously on two channels. Observation of simultaneous heteronuclear

259   and homonuclear polarization transfers as well as long range contacts were observed in 2D (H)NH spectra

260   using HET-RFDR for the microcrystalline protein SH3 using α-PET labeling. The comparison of 1D

261   HET-RFDR with CP followed by homonuclear RFDR showed similar efficiency of both methods at long

262   mixing times of about 3ms and longer. We experimentally and numerically demonstrated the dependence

263   of the HET-RFDR efficiency on the offset difference between dipolar coupled spins. A numerical

264   operator analysis of both HET-RFDR and RFDR sequences showed that when the offest difference was

265   small with respect to the MAS frequency, and with measurement at a whole number of rotor periods, the

266   behavior of HET-RFDR was similar to the well-known homonuclear RFRD. However, different

267   behaviors were observed when the offset difference could not be neglected.

268   Considering the evoultion of a single crystal during HET-RFDR and RFDR, we showed the

269   operators that were responsible for the transfer. We demostrated that XY phase cycling of π-pulses has a

270   crucial role for both HET-RFDR and RFDR transfer. With phase cycling of XX (or X$\overline{X}$) the transfers

271   between heteronuclear and homonuclear spins did not occur in the absence of offsets. With the presence

272   of the offset differences when they cannot be neglected in comparison to the MAS rate, RFDR

273   polarization transfer with phase cycling of XX or X$\overline{X}$ does occur, although with lower efficiency as was

274   described before (Bennett et al., 1992).

Experimental methods

276 *Sample preparation*: Microcrystalline chicken alpha spectrin SH3 protein was used for acquisition of all

277 experimental data. The samples were labeled with 100% protonation at exchangeable sites and either with

278 alpha proton exchange by transamination (α-PET) or with uniform ^{13}C and ^{15}N labeling with the protocol

279 described in (Movellan et al., 2019).

280 *Simulations*: HET-RFDR and RFDR simulations were performed with in-house MATLAB scripts using

281 numerical solution of the equation of motion (Nimerovsky and Goldbourt, 2012).

282 *Solid state NMR spectroscopy*: The HC and (H)N(H)H spectra of α-PET SH3 were acquired at 14.1 T (600

283 MHz) using a Bruker AVIIIHD spectrometer using a MASDVT600W2 BL1.3 HXY probe. The

284 experiments were performed at 10 kHz and 55.555 kHz MAS with the temperature of the cooling gas set

285 to 280 K and 235 K, respectively.

286 For 1D and 2D α-PET SH3 (H)N(H)H spectra, the ramped CP transfer from proton to nitrogen was

287 performed under the same conditions for all experiments: 42.95 kHz on the nitrogen channel and the optimal

288 ramped amplitude on the proton channel of 86.95-108.69 kHz. The mixing time was 1.05 ms. 9.3 kHz

289 WALTZ-16 (Shaka et al., 1983) with 25 us pulses and 10.4 kHz WALTZ-16 (Shaka et al., 1983) with 100

290 us pulses were applied on nitrogen and carbon channels during the acquisition. MISSISSIPPI water

291 suppression (Zhou and Rienstra, 2008) was applied for 100 ms with 13.513 kHz of the rf-field. The carrier

292 positions were set to 4.6 ppm, 118.5 ppm and 53.7 ppm for ^{1}H, ^{15}N and ^{13}C, respectively, except where

293 otherwise indicated.

294 Table 1 summarizes the applied experimental parameters for 1D spectra.

295 **Table 1** Summary of the experimental parameters used in the 1D CP + RFDR (the start and the end values are shown) and HET-

296 RFDR using α-PET labeled SH3.

	CP + RFDR		HET-RFDR
	CP	RFDR	
^{1}H (kHz)	86.95-108.69	86.21	86.21
^{15}N (kHz)	42.95	-	75.75
transfer time (ms)	0.55	[0-7.776]	[0-7.776]

NS	32	32
D1 (s)	2	2
AQ (s)	0.020448	0.020448
SW (kHz)	25	25

297   NS – number of scans; D1 – a recycle delay; AQ – the acquisition time; SW – the spectral width.

298   For 2D (H)N(H)H HET-RFDR spectra, during the indirect dimension 11.6 kHz SW_f-TPPM (Thakur et al.,

299   2006) decoupling with 36.36 us pulses was applied on the proton channel. Two mixing times were used:

300   1.152 ms and 3.456 ms. The widths of π-pulses on proton and nitrogen channels were 5.8 us and 6.6 us,

301   respectively. 16 scans were acquired per increment in t_1. The total time for the single 2D experiment was

302   10 hours. Table 2 summarizes the rest of the parameters.

303   **Table 2** Summary of the experimental parameters used in 2D HET HET-RFDR α-PET SH3 experiments.

	AQ1; AQ2 (s)	SW1; SW2 (kHz)	DW1; DW2 (us)
HET-RFDR	0.0527075; 0.020448	9.713; 25	102.94 20

304   1 and 2 are indirect and direct dimensions; AQ – the acquisition time; SW – the spectral width; DW – the dwell time.

305   2D CP + RFDR experiment with 1.152 and 3.456 ms of mixing time (only 1D slices are shown in Figure

306   2b) was performed with the same experimental conditions as 2D HET-RFDR. The CP mixing times from

307   H to N and from N to H were 1.05 ms and 0.55 ms, respectively.

308   For all 1D HC HET-RFDR experiments (Figure 3), 4.8 ms of the mixing time was applied. The widths of

309   π-pulses on proton and carbon channels were 5.8 us (86.21 kHz) and 6.6 us (75.75 kHz), respectively. 87

310   kHz SPINAL64 (Fung et al., 2000) with 6 us pulses was used during the acquisition. 128 scans were

311   accumulated. The spectral width was 50 kHz and the acquisition time 0.01536 s.

312   **Author Contributions**

313   EN performed the simulations and discovered HET-RFDR. EN and LBA designed experiments. EN and

314   KX recorded data. EN and LBA wrote the article. KTM prepared the SH3 protein samples. All authors

315   edited and approved the article.

316   **Competing Interests**

317   The authors declare that they have no conflict of interest.

321   **References**

322   Andreas, L. B., Le Marchand, T., Jaudzems, K., and Pintacuda, G.: High-resolution proton-detected NMR
323   of proteins at very fast MAS, J. Magn. Reson., 253, 36–49, https://doi.org/10.1016/j.jmr.2015.01.003,
324   2015.

325   Aucoin, D., Camenares, D., Zhao, X., Jung, J., Sato, T., and Smith, S. O.: High resolution 1H MAS RFDR
326   NMR of biological membranes, J. Magn. Reson. San Diego Calif 1997, 197, 77–86,
327   https://doi.org/10.1016/j.jmr.2008.12.009, 2009.

328   Bak, M., Rasmussen, J. T., and Nielsen, N. C.: SIMPSON : A General Simulation Program for Solid-State
329   NMR Spectroscopy, J. Magn. Reson. San Diego Calif 1997, 1–35,
330   https://doi.org/10.1006/jmre.2000.2179, 2000.

331   Bennett, A. E., Griffin, R. G., Ok, J. H., and Vega, S.: Chemical shift correlation spectroscopy in rotating
332   solids: Radio frequency-driven dipolar recoupling and longitudinal exchange, J. Chem. Phys., 96, 8624–
333   8627, https://doi.org/10.1063/1.462267, 1992.

334   Bennett, A. E., Rienstra, C. M., Griffiths, J. M., Zhen, W., Lansbury, P. T., and Griffin, R. G.: Homonuclear
335   radio frequency-driven recoupling in rotating solids, J. Chem. Phys., 108, 9463–9479,
336   https://doi.org/10.1063/1.476420, 1998.

337   Brinkmann, A. and Levitt, M. H.: Symmetry principles in the nuclear magnetic resonance of spinning
338   solids: Heteronuclear recoupling by generalized Hartmann–Hahn sequences, J. Chem. Phys., 115, 357–
339   384, https://doi.org/10.1063/1.1377031, 2001.

340   Brinkmann, A., Schmedt auf der Günne, J., and Levitt, M. H.: Homonuclear Zero-Quantum Recoupling in
341   Fast Magic-Angle Spinning Nuclear Magnetic Resonance, J. Magn. Reson., 156, 79–96,
342   https://doi.org/10.1006/jmre.2002.2525, 2002.

343   Carravetta, M., Edén, M., Zhao, X., Brinkmann, A., and Levitt, M. H.: Symmetry principles for the design
344   of radiofrequency pulse sequences in the nuclear magnetic resonance of rotating solids, Chem. Phys.
345   Lett., 321, 205–215, https://doi.org/10.1016/S0009-2614(00)00340-7, 2000.

346   Castellani, F., van Rossum, B., Diehl, A., Schubert, M., Rehbein, K., and Oschkinat, H.: Structure of a
347   protein determined by solid-state magic-angle-spinning NMR spectroscopy, Nature, 420, 99–102,
348   https://doi.org/10.1038/nature01070, 2002.

349 Colvin, M. T., Silvers, R., Frohm, B., Su, Y., Linse, S., and Griffin, R. G.: High Resolution Structural
350 Characterization of Aβ42 Amyloid Fibrils by Magic Angle Spinning NMR, J. Am. Chem. Soc., 137, 7509–
351 7518, https://doi.org/10.1021/jacs.5b03997, 2015.

352 Daskalov, A., Martinez, D., Coustou, V., Mammeri, N. E., Berbon, M., Andreas, L. B., Bardiaux, B., Stanek,
353 J., Noubhani, A., Kauffmann, B., Wall, J. S., Pintacuda, G., Saupe, S. J., Habenstein, B., and Loquet, A.:
354 Structural and molecular basis of cross-seeding barriers in amyloids, bioRxiv, 2020.07.06.188508,
355 https://doi.org/10.1101/2020.07.06.188508, 2020.

356 Ernst, R. R., Bodenhausen, G., and Wokaun, A.: Principles of nuclear magnetic resonance in one and two
357 dimensions, Oxford Univ. Press, London/New York, 610 pp., 1987.

358 Fritz, M., Kraus, J., Quinn, C. M., Yap, G. P. A., Struppe, J., Sergeyev, I. V., Gronenborn, A. M., and
359 Polenova, T.: Measurement of Accurate Interfluorine Distances in Crystalline Organic Solids: A High-
360 Frequency Magic Angle Spinning NMR Approach, J. Phys. Chem. B, 123, 10680–10690,
361 https://doi.org/10.1021/acs.jpcb.9b08919, 2019.

362 Fung, B. M., Khitrin, A. K., and Ermolaev, K.: An Improved Broadband Decoupling Sequence for Liquid
363 Crystals and Solids, J. Magn. Reson., 142, 97–101, https://doi.org/10.1006/jmre.1999.1896, 2000.

364 Gelenter, M. D. and Hong, M.: Efficient 15N–13C Polarization Transfer by Third-Spin-Assisted Pulsed
365 Cross-Polarization Magic-Angle-Spinning NMR for Protein Structure Determination, J. Phys. Chem. B,
366 122, 8367–8379, https://doi.org/10.1021/acs.jpcb.8b06400, 2018.

367 Gelenter, M. D., Dregni, A. J., and Hong, M.: Pulsed Third-Spin-Assisted Recoupling NMR for Obtaining
368 Long-Range 13C–13C and 15N–13C Distance Restraints, J. Phys. Chem. B, 124, 7138–7151,
369 https://doi.org/10.1021/acs.jpcb.0c04574, 2020.

370 Grohe, K., Nimerovsky, E., Singh, H., Vasa, S. K., Söldner, B., Voegeli, B., Rienstra, C. M., and Linser, R.:
371 Exact distance measurements for structure and dynamics in solid proteins by fast-magic-angle-spinning
372 NMR, Chem. Commun., https://doi.org/10.1039/C9CC02317H, 2019.

373 Gullion, T. and Schaefer, J.: Rotational-echo double-resonance NMR, J. Magn. Reson. 1969, 81, 196–200,
374 https://doi.org/10.1016/0022-2364(89)90280-1, 1989.

375 Gullion, T. and Vega, S.: A simple magic angle spinning NMR experiment for the dephasing of rotational
376 echoes of dipolar coupled homonuclear spin pairs, Chem. Phys. Lett., 194, 423–428,
377 https://doi.org/10.1016/0009-2614(92)86076-T, 1992.

378 Gullion, T., Baker, D. B., and Conradi, M. S.: New, compensated Carr-Purcell sequences, J. Magn. Reson.
379 1969, 89, 479–484, https://doi.org/10.1016/0022-2364(90)90331-3, 1990.

380 Haeberlen, U. and Waugh, J. S.: Coherent Averaging Effect in Magnetic Resonance, Phys. Rev., 175, 453–
381 467, https://doi.org/10.1103/PhysRev.175.453, 1968.

382 Hartmann, S. R. and Hahn, E. L.: Nuclear Double Resonance in the Rotating Frame, Phys. Rev., 128,
383 2042–2053, https://doi.org/10.1103/PhysRev.128.2042, 1962.

384 Hediger, S., Meier, B. H., Kurur, N. D., Bodenhausen, G., and Ernst, R. R.: NMR cross polarization by
385 adiabatic passage through the Hartmann—Hahn condition (APHH), Chem. Phys. Lett., 223, 283–288,
386 https://doi.org/10.1016/0009-2614(94)00470-6, 1994.

387 Hellwagner, J., Wili, N., Ibáñez, L. F., Wittmann, J. J., Meier, B. H., and Ernst, M.: Transient effects in π-
388 pulse sequences in MAS solid-state NMR, J. Magn. Reson., 287, 65–73,
389 https://doi.org/10.1016/j.jmr.2017.12.015, 2018.

390 Hing, A. W., Vega, S., and Schaefer, J.: Transferred-echo double-resonance NMR, J. Magn. Reson. 1969,
391 96, 205–209, https://doi.org/10.1016/0022-2364(92)90305-Q, 1992.

392 Hou, G., Byeon, I.-J. L., Ahn, J., Gronenborn, A. M., and Polenova, T.: 1H–13C/1H–15N Heteronuclear
393 Dipolar Recoupling by R-Symmetry Sequences Under Fast Magic Angle Spinning for Dynamics Analysis of
394 Biological and Organic Solids, J. Am. Chem. Soc., 133, 18646–18655, https://doi.org/10.1021/ja203771a,
395 2011a.

396 Hou, G., Yan, S., Sun, S., Han, Y., Byeon, I.-J. L., Ahn, J., Concel, J., Samoson, A., Gronenborn, A. M., and
397 Polenova, T.: Spin Diffusion Driven by R-Symmetry Sequences: Applications to Homonuclear Correlation
398 Spectroscopy in MAS NMR of Biological and Organic Solids, J. Am. Chem. Soc., 133, 3943–3953,
399 https://doi.org/10.1021/ja108650x, 2011b.

400 Hou, G., Yan, S., Trébosc, J., Amoureux, J.-P., and Polenova, T.: Broadband homonuclear correlation
401 spectroscopy driven by combined R2nv sequences under fast magic angle spinning for NMR structural
402 analysis of organic and biological solids, J. Magn. Reson., 232, 18–30,
403 https://doi.org/10.1016/j.jmr.2013.04.009, 2013.

404 Ishii, Y.: 13C–13C dipolar recoupling under very fast magic angle spinning in solid-state nuclear magnetic
405 resonance: Applications to distance measurements, spectral assignments, and high-throughput
406 secondary-structure determination, J. Chem. Phys., 114, 8473–8483,
407 https://doi.org/10.1063/1.1359445, 2001.

408 Jain, M. G., Lalli, D., Stanek, J., Gowda, C., Prakash, S., Schwarzer, T. S., Schubeis, T., Castiglione, K.,
409 Andreas, L. B., Madhu, P. K., Pintacuda, G., and Agarwal, V.: Selective 1H–1H Distance Restraints in Fully
410 Protonated Proteins by Very Fast Magic-Angle Spinning Solid-State NMR, J. Phys. Chem. Lett., 8, 2399–
411 2405, https://doi.org/10.1021/acs.jpclett.7b00983, 2017.

412 Jaroniec, C. P., Filip, C., and Griffin, R. G.: 3D TEDOR NMR Experiments for the Simultaneous
413 Measurement of Multiple Carbon–Nitrogen Distances in Uniformly 13C,15N-Labeled Solids, J. Am.
414 Chem. Soc., 124, 10728–10742, https://doi.org/10.1021/ja026385y, 2002.

415 Ji, Y., Liang, L., Guo, C., Bao, X., Polenova, T., and Hou, G.: Zero-Quantum Homonuclear Recoupling
416 Symmetry Sequences in Solid-State Fast MAS NMR Spectroscopy, Acta Phys.-Chim. Sin., 36, 1905029–
417 1905034, 2020.

418 Linser, R., Bardiaux, B., Andreas, L. B., Hyberts, S. G., Morris, V. K., Pintacuda, G., Sunde, M., Kwan, A. H.,
419 and Wagner, G.: Solid-State NMR Structure Determination from Diagonal-Compensated, Sparsely
420 Nonuniform-Sampled 4D Proton–Proton Restraints, J. Am. Chem. Soc., 136, 11002–11010,
421 https://doi.org/10.1021/ja504603g, 2014.

Maricq, M. M.: Application of average hamiltonian theory to the NMR of solids, Phys. Rev. B, 25, 6622–6632, https://doi.org/10.1103/PhysRevB.25.6622, 1982.

Mehring, M.: Principles of High Resolution NMR in Solids, 2nd ed., Springer-Verlag, Berlin Heidelberg, https://doi.org/10.1007/978-3-642-68756-3, 1983.

Meier, B. H. and Earl, W. L.: Excitation of multiple quantum transitions under magic angle spinning conditions: Adamantane, J. Chem. Phys., 85, 4905–4911, https://doi.org/10.1063/1.451726, 1986.

Messinger, R. J., Ménétrier, M., Salager, E., Boulineau, A., Duttine, M., Carlier, D., Ateba Mba, J.-M., Croguennec, L., Masquelier, C., Massiot, D., and Deschamps, M.: Revealing Defects in Crystalline Lithium-Ion Battery Electrodes by Solid-State NMR: Applications to LiVPO4F, Chem. Mater., 27, 5212–5221, https://doi.org/10.1021/acs.chemmater.5b01234, 2015.

Metz, G., Wu, X. L., and Smith, S. O.: Ramped-Amplitude Cross Polarization in Magic-Angle-Spinning NMR, J. Magn. Reson. A, 110, 219–227, https://doi.org/10.1006/jmra.1994.1208, 1994.

Movellan, K. T., Najbauer, E. E., Pratihar, S., Salvi, M., Giller, K., Becker, S., and Andreas, L. B.: Alpha protons as NMR probes in deuterated proteins, J. Biomol. NMR, 73, 81–91, https://doi.org/10.1007/s10858-019-00230-y, 2019.

Nielsen, N. Chr., Strassø, L. A., and Nielsen, A. B.: Dipolar Recoupling, in: Solid State NMR, edited by: Chan, J. C. C., Springer, Berlin, Heidelberg, 1–45, https://doi.org/10.1007/128_2011_129, 2012.

Nimerovsky, E. and Goldbourt, A.: Insights into the spin dynamics of a large anisotropy spin subjected to long-pulse irradiation under a modified REDOR experiment., J. Magn. Reson., 225, 130–41, https://doi.org/10.1016/j.jmr.2012.09.015, 2012.

Nishiyama, Y., Malon, M., Ishii, Y., and Ramamoorthy, A.: 3D 15N/15N/1H chemical shift correlation experiment utilizing an RFDR-based 1H/1H mixing period at 100kHz MAS, J. Magn. Reson., 244, 1–5, https://doi.org/10.1016/j.jmr.2014.04.008, 2014a.

Nishiyama, Y., Zhang, R., and Ramamoorthy, A.: Finite-pulse radio frequency driven recoupling with phase cycling for 2D 1H/1H correlation at ultrafast MAS frequencies, J. Magn. Reson., 243, 25–32, https://doi.org/10.1016/j.jmr.2014.03.004, 2014b.

Ok, J. H., Spencer, R. G. S., Bennett, A. E., and Griffin, R. G.: Homonuclear correlation spectroscopy in rotating solids, Chem. Phys. Lett., 197, 389–395, https://doi.org/10.1016/0009-2614(92)85790-H, 1992.

Olejniczak, E. T., Vega, S., and Griffin, R. G.: Multiple pulse NMR in rotating solids, J. Chem. Phys., 81, 4804–4817, https://doi.org/10.1063/1.447506, 1984.

Pandey, M. K. and Nishiyama, Y.: A one-dimensional solid-state NMR approach for 14NH/14NH overtone correlation through 1H/1H mixing under fast MAS, Phys. Chem. Chem. Phys., 20, 25849–25853, https://doi.org/10.1039/C8CP05000G, 2018.

Pandey, M. K., Vivekanandan, S., Yamamoto, K., Im, S., Waskell, L., and Ramamoorthy, A.: Proton-detected 2D radio frequency driven recoupling solid-state NMR studies on micelle-associated cytochrome-b5, J. Magn. Reson., 242, 169–179, https://doi.org/10.1016/j.jmr.2014.02.016, 2014.

Petkova, A. T., Ishii, Y., Balbach, J. J., Antzutkin, O. N., Leapman, R. D., Delaglio, F., and Tycko, R.: A structural model for Alzheimer's -amyloid fibrils based on experimental constraints from solid state NMR, Proc. Natl. Acad. Sci., 99, 16742–16747, https://doi.org/10.1073/pnas.262663499, 2002.

Roos, M., Mandala, V. S., and Hong, M.: Determination of Long-Range Distances by Fast Magic-Angle-Spinning Radiofrequency-Driven 19F–19F Dipolar Recoupling NMR, J. Phys. Chem. B, 122, 9302–9313, https://doi.org/10.1021/acs.jpcb.8b06878, 2018.

Rovnyak, D.: Tutorial on analytic theory for cross-polarization in solid state NMR, Concepts Magn. Reson. Part A, 32A, 254–276, https://doi.org/10.1002/cmr.a.20115, 2008.

Saalwächter, K.: Robust NMR Approaches for the Determination of Homonuclear Dipole–Dipole Coupling Constants in Studies of Solid Materials and Biomolecules, ChemPhysChem, 14, 3000–3014, https://doi.org/10.1002/cphc.201300254, 2013.

Shaka, A. J., Keeler, J., Frenkiel, T., and Freeman, R.: An improved sequence for broadband decoupling: WALTZ-16, J. Magn. Reson. 1969, 52, 335–338, https://doi.org/10.1016/0022-2364(83)90207-X, 1983.

Shen, M., Hu, B., Lafon, O., Trébosc, J., Chen, Q., and Amoureux, J.-P.: Broadband finite-pulse radio-frequency-driven recoupling (fp-RFDR) with (XY8)41 super-cycling for homo-nuclear correlations in very high magnetic fields at fast and ultra-fast MAS frequencies, J. Magn. Reson., 223, 107–119, https://doi.org/10.1016/j.jmr.2012.07.013, 2012.

Shi, C., Fricke, P., Lin, L., Chevelkov, V., Wegstroth, M., Giller, K., Becker, S., Thanbichler, M., and Lange, A.: Atomic-resolution structure of cytoskeletal bactofilin by solid-state NMR, Sci. Adv., 1, https://doi.org/10.1126/sciadv.1501087, 2015.

Slichter, C. P.: Principles of Magnetic Resonance, 3rd ed., Springer-Verlag, Berlin Heidelberg, https://doi.org/10.1007/978-3-662-09441-9, 1990.

Sun, B. Q., Costa, P. R., and Griffin, R. G.: Heteronuclear Polarization Transfer by Radiofrequency-Driven Dipolar Recoupling Under Magic-Angle Spinning, J. Magn. Reson. A, 112, 191–198, https://doi.org/10.1006/jmra.1995.1031, 1995.

Szeverenyi, N. M., Sullivan, M. J., and Maciel, G. E.: Observation of spin exchange by two-dimensional fourier transform 13C cross polarization-magic-angle spinning, J. Magn. Reson. 1969, 47, 462–475, https://doi.org/10.1016/0022-2364(82)90213-X, 1982.

Takegoshi, K., Nakamura, S., and Terao, T.: 13C–1H dipolar-assisted rotational resonance in magic-angle spinning NMR, Chem. Phys. Lett., 344, 631–637, https://doi.org/10.1016/S0009-2614(01)00791-6, 2001.

Tang, M., Berthold, D. A., and Rienstra, C. M.: Solid-State NMR of a Large Membrane Protein by Paramagnetic Relaxation Enhancement, J. Phys. Chem. Lett., 2, 1836–1841, https://doi.org/10.1021/jz200768r, 2011.

Thakur, R. S., Kurur, N. D., and Madhu, P. K.: Swept-frequency two-pulse phase modulation for heteronuclear dipolar decoupling in solid-state NMR, Chem. Phys. Lett., 426, 459–463, https://doi.org/10.1016/j.cplett.2006.06.007, 2006.

494   Tycko, R. and Dabbagh, G.: Measurement of nuclear magnetic dipole—dipole couplings in magic angle
495   spinning NMR, Chem. Phys. Lett., 173, 461–465, https://doi.org/10.1016/0009-2614(90)87235-J, 1990.

496   Wong, K. M., Wang, Y., Seroski, D. T., Larkin, G. E., Mehta, A. K., Hudalla, G. A., Hall, C. K., and Paravastu,
497   A. K.: Molecular complementarity and structural heterogeneity within co-assembled peptide β-sheet
498   nanofibers, Nanoscale, 12, 4506–4518, https://doi.org/10.1039/C9NR08725G, 2020.

499   Wu, X. L. and Zilm, K. W.: Cross Polarization with High-Speed Magic-Angle Spinning, J. Magn. Reson. A,
500   104, 154–165, https://doi.org/10.1006/jmra.1993.1203, 1993.

501   Zhang, R., Nishiyama, Y., Sun, P., and Ramamoorthy, A.: Phase cycling schemes for finite-pulse-RFDR
502   MAS solid state NMR experiments, J. Magn. Reson., 252, 55–66,
503   https://doi.org/10.1016/j.jmr.2014.12.010, 2015.

504   Zhang, R., Mroue, K. H., and Ramamoorthy, A.: Proton-Based Ultrafast Magic Angle Spinning Solid-State
505   NMR Spectroscopy, Acc. Chem. Res., 50, 1105–1113, https://doi.org/10.1021/acs.accounts.7b00082,
506   2017.

507   Zhang, Z., Chen, Y., and Yang, J.: Band-selective heteronuclear dipolar recoupling with dual back-to-back
508   pulses in rotating solids, J. Magn. Reson., 272, 46–52, https://doi.org/10.1016/j.jmr.2016.09.003, 2016.

509   Zhang, Z., Oss, A., Org, M.-L., Samoson, A., Li, M., Tan, H., Su, Y., and Yang, J.: Selectively Enhanced 1H–
510   1H Correlations in Proton-Detected Solid-State NMR under Ultrafast MAS Conditions, J. Phys. Chem.
511   Lett., 11, 8077–8083, https://doi.org/10.1021/acs.jpclett.0c02412, 2020.

512   Zheng, Z., Qiang, W., and Weliky, D. P.: Investigation of finite-pulse radiofrequency-driven recoupling
513   methods for measurement of intercarbonyl distances in polycrystalline and membrane-associated HIV
514   fusion peptide samples, Magn. Reson. Chem., 45, S247–S260, https://doi.org/10.1002/mrc.2160, 2007.

515   Zhou, D. H. and Rienstra, C. M.: High-performance solvent suppression for proton detected solid-state
516   NMR, J. Magn. Reson., 192, 167–172, https://doi.org/10.1016/j.jmr.2008.01.012, 2008.

517   Zhou, D. H., Nieuwkoop, A. J., Berthold, D. A., Comellas, G., Sperling, L. J., Tang, M., Shah, G. J., Brea, E.
518   J., Lemkau, L. R., and Rienstra, C. M.: Solid-state NMR analysis of membrane proteins and protein
519   aggregates by proton detected spectroscopy, J. Biomol. NMR, 54, 291–305,
520   https://doi.org/10.1007/s10858-012-9672-z, 2012.

521   Zinke, M., Fricke, P., Lange, S., Zinn-Justin, S., and Lange, A.: Protein–Protein Interfaces Probed by
522   Methyl Labeling and Proton-Detected Solid-State NMR Spectroscopy, Chemphyschem, 19, 2457–2460,
523   https://doi.org/10.1002/cphc.201800542, 2018.

524

525